# Demonstration of *in-vivo* multi-probe tracker based on a Si/CdTe semiconductor Compton camera

Shin'ichiro Takeda, Hirokazu Odaka, Shin-nosuke Ishikawa, Shin Watanabe
Hiroyuki Aono, Tadayuki Takahashi, Yousuke Kanayama, Makoto Hiromura and Shuichi Enomoto

***Abstract*—By using a prototype Compton camera consisting of silicon (Si) and cadmium telluride (CdTe) semiconductor detectors, originally developed for the ASTRO-H satellite mission, an experiment involving imaging multiple radiopharmaceuticals injected into a living mouse was conducted to study its feasibility for medical imaging. The accumulation of both iodinated ($^{131}$I) methylnorcholestenol and $^{85}$Sr into the mouse's organs was simultaneously imaged by the prototype. This result implies that the Compton camera is expected to become a multi-probe tracker available in nuclear medicine and small animal imaging.**

***Index Terms*—Astrophysics, Si/CdTe Semiconductor Compton camera, nuclear medicine, small animal imaging**

## I. Introduction

IN the fields of nuclear medicine and small animal imaging, a next-generation instrument capable of imaging a wide energy range and fine energy resolution, enabling emission lines to be precisely distinguished from different radioisotopes, is desirable. In diagnostic imaging, to detect cancer and recurrence inside the body is a critical issue. However, even with early detections by positron emission tomography (PET), it remains difficult to differentiate between benign and malignant lesions at various stages. In order to characterize cancers and their surrounding environment which leads to the improvement of diagnostic accuracy, and to decide the most appropriate treatment strategy, diagnosis by means of multiple probes is required to provide more comprehensive information. However, such an approach has not been realized by PET since it only allows tracking of a single positron-emitting probe.

The high energy resolution and sufficient efficiency at a few hundred keV band are the key to realize the multi-probe tracker, and there seems to be two prospective approaches. One is the use of semiconductor SPECT camera against a backdrop of recent progresses in new semiconductor imagers represented by cadmium telluride (CdTe) and cadmium zinc telluride (CZT) detectors, which have high stopping power in comparison with silicon (Si) and germanium (Ge). Fine energy resolution realized by the detectors ($\Delta E/E \sim 1$ %) enables gamma-ray lines emitted from various kinds of RIs to be detected, which was previously impossible when using traditional NaI scintillation detectors. Some instruments have begun to appear in the market [1], [2]. However, the upper energy range is limited due to use of mechanical collimator (up to 364 keV from $^{131}$I ), hence the selection of labeled RIs is also limited to a few varieties such as $^{99m}$Tc (140 keV), $^{123}$I (159 keV) or $^{111}$In (171 keV). Another approach is a semiconductor Compton camera, which is described in this paper. The Compton camera detects the Compton scattering process for image reconstruction, while the SPECT camera detects the photo absorption process. Because the mechanical collimator is not required in Compton imaging, the camera can image in a wider energy band and covers many kinds of RIs, including SPECT and PET probes, making it the most versatile imaging system for use in the multi-probe tracker.

It has been demonstrated that a semiconductor Compton camera by using germanium detectors has high potential to make individual images from deferent emission lines. Motomura et al. [3] has shown simultaneous images of multiple radiopharmaceuticals injected into a living mouse. However, since the system needs to operate at around liquid nitrogen temperature, it would be difficult to make compact and portable system, which would be needed in practical situation. Therefore, it is desirable to develop a semiconductor Compton camera which can be operated at around room temperature. In this paper, we report the first result of experiments involving imaging radiopharmaceuticals with a new Si/CdTe Compton camera, consisting of multiple layers of Si and CdTe imaging detectors. After we describe the set up and analysis procedure, we present the imaging performance.

## II. The prototype camera

ISAS/JAXA group, a Japanese space science research institute, has developed a Si/CdTe Compton camera [4], [5] for the ASTRO-H satellite mission scheduled for launch in 2014 [6], [7]. Because details of the detector configuration and data acquisition for the prototype camera are reported in Takeda et al. [8], we briefly explain the system.

The camera consists of a single layers of double-sided silicon strip detector (DSSD) and four layers of CdTe pixel detectors (see Fig. 1). The stacked CdTe module is placed 14.5 mm over the DSSD, in which each CdTe layer contains four CdTe detectors in a 2×2 arrangement. Table I summarizes the dimensions and typical performance of each DSSD and CdTe detector element. The detectors were operated at around -10 °C by circulating cooled liquid ethylene glycol through aluminum detector box.

In the Si/CdTe Compton camera, the events involving the incident gamma-ray being scattered in the Si detector and fully

S.Takeda, H. Odaka, S. Ishikawa, S. Watanabe and T. Takahashi are members of the Institute of Space and Astronautical Science, Japan Aerospace Exploration Agency, 3-1-1 Yoshinodai Sagamihara Kanagawa 229-8510, Japan, and also the Department of Physics, The University of Tokyo, 7-3-1 Hongo Bunkyo-ku Tokyo 113-0033, Japan (E-mail: takeda@astro.isas.jaxa.jp)

S.Takeda, Y. Kanayama, Makoto Hiromura and S. Enomoto are with the RIKEN Center for Molecular Imaging Science, 6-7-3 Minatojima Minami-machi, Chuo-ku, Kobe, Hyogo 650-0047, Japan

| Detector | Active Area [mm] | Thickness [mm] | Strip pitch (Pixel size) [mm] | Bias [V] | Energy resolution |
|---|---|---|---|---|---|
| DSSD (Si) | 25.6 × 25.6 | 0.5 | 0.4 | 250 | 1.6 keV (FWHM) at 59.5 keV |
| CdTe pixel | 13.2 × 13.2 | 0.5 | 1.35 | 600 | 2.0 keV (FWHM) at 81 keV<br>ΔE/E ∼1 % (FWHM) at 511 keV |

TABLE I
DIMENSIONS, OPERATING BIAS VOLTAGES, ENERGY RESOLUTIONS FOR DSSD AND CDTE DETECTORS.

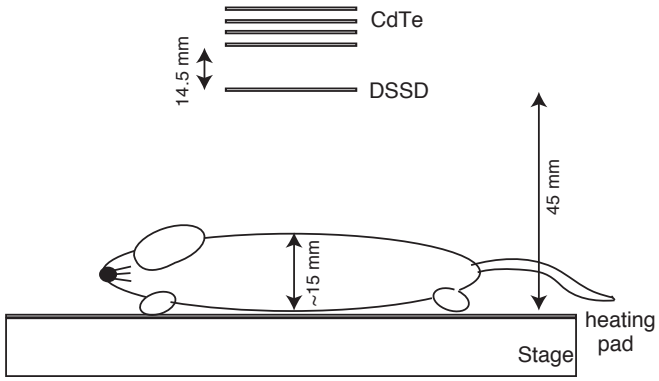


Fig. 1. Setup of mouse imaging as described in section IV. The camera consists of a single layer of the DSSD and four layers of CdTe pixel detectors. The distance between the mouse and camera is about 30 mm.

absorbed in the CdTe detectors are used for Compton imaging. Since the effect of the Doppler broadening is smaller in the Si devices than other semiconductor devices [9], the camera allows the difference between the measured and actual scattering angles to be constrained, meaning higher position resolution is expected. Therefore, the coincidence trigger measurement between DSSD and CdTe pixel detectors is performed for effective data acquisition. The trigger thresholds are set to around 30 and 20 keV for DSSD and CdTe pixel detectors, respectively.

## III. DATA ANALYSIS

We study near-field Compton imaging by using the data of two point sources, $^{133}$Ba (356 keV, 2.8 MBq) and $^{22}$Na (511 keV, 1.3 MBq), located at a 30 mm plane from the detector surface (see the upper panel of Fig.9).

### A. Event selection

To image using the Compton camera, we first have to search the list mode data to find candidates of the Compton event, in which gamma-rays are scattered in the Si part and fully absorbed in the CdTe part. The goal of this event selection is to determine the energy transported to an electron $E'_e$ and the energy of the scattered gamma-ray $E'_\gamma$ in order to solve the scattering angle $\theta$ with the Compton kinematics;

$$\cos\theta = 1 - m_e c^2 \Big( \frac{1}{E'_\gamma} - \frac{1}{E'_e + E'_\gamma} \Big). \quad (1)$$

In addition, both the scattering position and the direction of the scattered gamma-ray $\vec{S}$ are required for the back-projection (see Section III-B). The steps for the event selection are shown in Fig. 2.

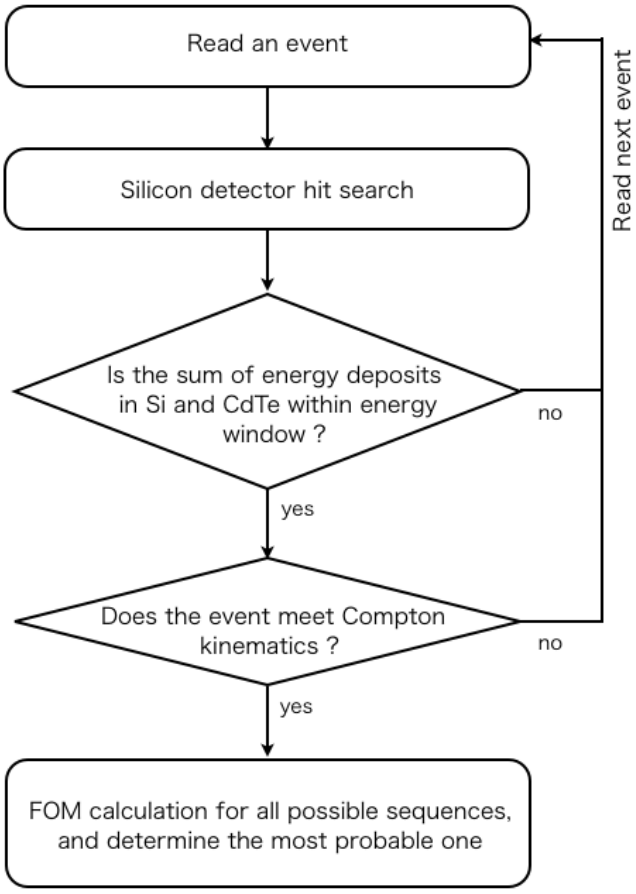


Fig. 2. Event selection flow

After reading an event which comprises the pulse heights of all detector channels, the first step involves determining the hit in the DSSD to obtain the scattering position and its energy deposit. Here, we search the strips recording peak energy in each Pside and Nside, and if the peak energies on each side exceed the threshold of 10 keV, we decide the hit in the DSSD. The x-y position of the hit is determined from the configuration of the P and N strips, and the z position is assigned to the center of depth of the DSSD. The energy deposit is determined by the Pside pulse height because the Pside has better energy resolution than the Nside. This energy deposit is the energy transported to an electron $E'_e$.

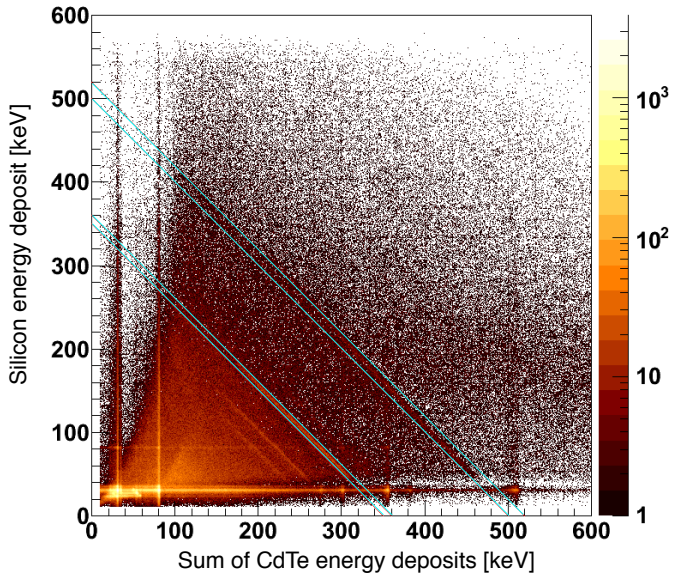


Fig. 3. A two-dimensional scatter plot of Si and CdTe energy deposits. The energy deposits in the CdTe part are added.

Having obtained the scattering position and $E'_e$, the direction and energy of scattered gamma-ray ($\vec{S}$ and $E'_\gamma$) provide complete information for the back-projection. The $E'_\gamma$ is obtained by adding the energy deposits in the CdTe part. Before the calculation of $\vec{S}$, we apply the energy window selection to image the distribution of multiple radioisotopes individually. Figure 3 shows a two-dimensional scatter plot of Si and CdTe energy deposits by locating two point sources of $^{133}$Ba (356 keV) and $^{22}$Na (511 keV) in front of the camera. The energy deposits in the CdTe part are added. A structure in which the energy sum of Si and CdTe are equal to the input energies of 356 and 511 keV contains fully energy deposited Compton events, hence we use the events within the energy window drawn with cyan lines, which correspond to 350–360 and 500–520 keV, in the following analysis.

In addition to the energy window selection, we also apply the selection derived from Compton kinematics. Because the right-hand side of Eq.(1) must be between $-1$ and 1, we otherwise skip the following analysis and read the next event.

Here, we have already obtained the energy transported to an electron $E'_e$, the scattering position in the DSSD, and the energy of the scattered gamma-ray $E'_\gamma$. The final step involves calculating the direction of the scattered gamma-ray $\vec{S}$. If the number of hits in the CdTe part is one, the direction is simply calculated by connecting the scattering position in the DSSD and the hit's position in the CdTe. Figure 4 shows the multiplicity of the CdTe part for the event inside the energy window of 350–360 and 500–520 keV. Although 70–75% of all events are distributed as a single hit in the CdTe part, extended analysis of multiple hits, which originate from multiple Compton scattering in the CdTe part, could increase the detection efficiency by about one and a half times. One difficulty is that the inability to time-of-flight measurement due to the short distance of the detectors means we cannot directly determine the interaction sequence in the CdTe part. We attempted the following figure of merit (FOM) analysis.

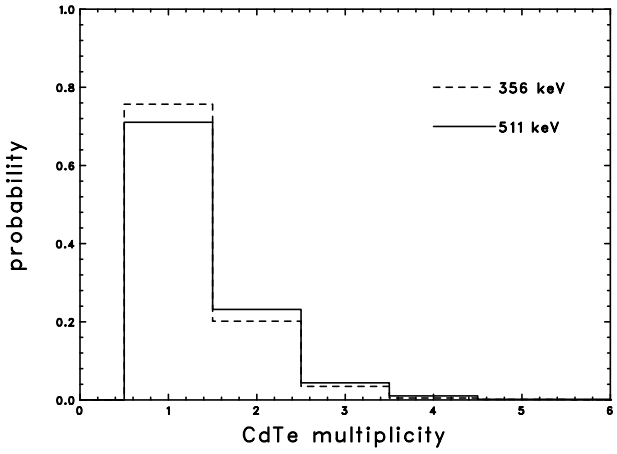


Fig. 4. The multiplicity of the CdTe part for the event inside the energy windows of 350–360 and 500–520 keV drawn in Fig.3

N! of sequences are possible for N hits in the CdTe part. The FOM analysis uses the fact that the scattering angle $\phi$ in the diagram of Fig. 5 is also calculated by energetic information. Here, we define $[\phi|t]$ and $[\phi|e]$ for the topological and energetic scattering angle, respectively. The $[\phi|t]$ corresponds to the $\phi$ in the diagram, while the $[\phi|e]$ is calculated by the energy deposit at the reference point and the sum of the following energy deposits in sequence with Compton kinematics as described in Eq. (1). Since N-hits provides a total of $(N-1)$ calculations of $[\phi|t]$ and $[\phi|e]$, the FOM for a certain sequence could be defined as;

$$FOM = \sum_i^{N-1} \frac{([\phi|t]_i - [\phi|e]_i)^2}{(\Delta[\phi|t]_i)^2 + (\Delta[\phi|e]_i)^2} \qquad (2)$$

The most probable sequence is expected to minimize the FOM value. Once the most probable sequence is determined, the $\vec{S}$ is derived from the scattering position in the DSSD and the first interaction position in the CdTe part. In practical terms, since the multi-hit event with $N > 5$ is negligible, we skip the analysis in that case. The scope of this paper does not include the $\phi$-dependance of $\Delta[\phi|t]$ and $\Delta[\phi|e]$.

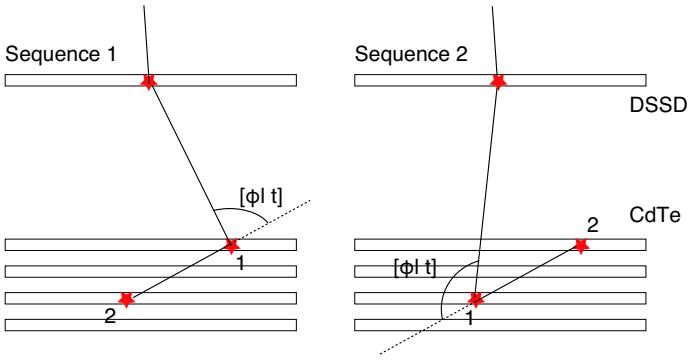


Fig. 5. Possible sequences for N=2. Here, N is the number of the hits in the CdTe part.

In the multi-hit analysis, the calculation of $E'_\gamma$ by adding the energy deposits in the CdTe part should be reconsidered.

By applying error propagation to Eq.(1)

$$(\Delta\theta)^2 = \left[\frac{m_e c^2}{\sin\theta}\frac{1}{(E'_e+E'_\gamma)^2}\right]^2(\Delta E'_e)^2 + \left[\frac{m_e c^2}{\sin\theta}\Big(\frac{1}{(E'_e+E'_\gamma)^2}-\frac{1}{E'^2_\gamma}\Big)\right]^2(\Delta E'_\gamma)^2 \quad (3)$$

is given. Therefore, in the case of known energy $E_\gamma$, the subtraction by $E'_\gamma = E_\gamma - E'_e$ provides better angular resolution than the addition because the increase of $\Delta E'_\gamma$ is constrained.

### B. Near-field back-projection

Unlike astrophysical observation, the targets are located in the near-field in medical imaging, meaning the direction of the incident gamma-ray, as calculated by the parameters derived in section III-A, should be projected in three-dimensional space. We describe our back-projection method and experimental verification in this section.

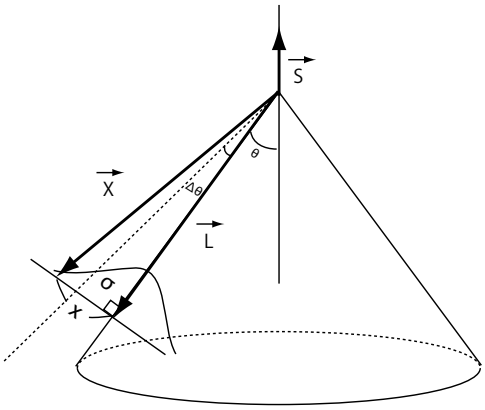


Fig. 6. Diagram of the three-dimensional back-projection

Figure 6 shows the diagram of the three-dimensional back-projection. The back-projection cone is drawn from the starting point of the direction vector $\vec{S}$, where the angle of the cone $\theta$ is calculated by Compton kinematics of Eq.(1). Due to the uncertainty originating from the incomplete position, energy measurement with a real detector and the Doppler broadening effect, the $\theta$ contains uncertainty. Therefore, with increasing distance, the cone profile shows a wider spread. To consider the spread, we define the voxel value $V(\vec{X})$ at the reference point vector $\vec{X}$ (voxel center) as follows;

$$V(\vec{X}) = |\vec{L}|^{-w}\exp\Big[-\frac{1}{2}\Big(\frac{x}{\sigma}\Big)^2\Big] \quad (4)$$

here,

$$x = |\vec{X}-\vec{L}| \quad (5)$$

$$\sigma = |\vec{L}|\tan(\Delta\theta). \quad (6)$$

where, $\Delta\theta$ is the parameter for angular uncertainty and $w$ is the weighting parameter for the distance $|\vec{L}|$. Typically, the value of $\Delta\theta$ in our camera is around 1 degree. We adopt a Gaussian distribution to express the cone spread in this study. Practically, to avoid loss of time in the back-projection process, we limited the back-projection region to $3\times\Delta\theta$ and applied the Source Space Tree Algorithm (SSTA) [10] to our cone spread projection. Briefly, the SSTA provides an effective voxel search by dividing the back-projection space into successively smaller subdivisions, testing for cone-surface interception at each subdivision branch level, until the subdivision regions are identical with the voxels.

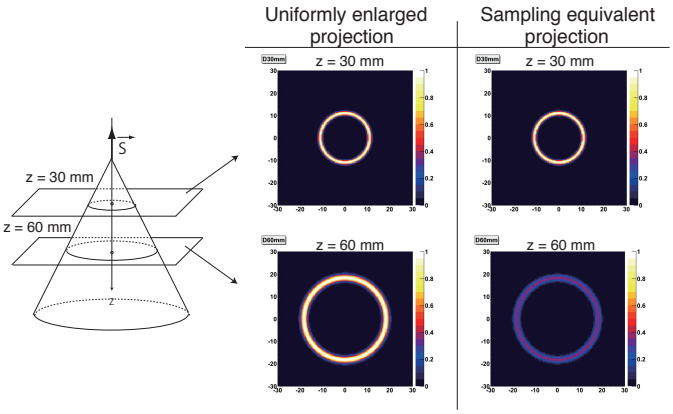


Fig. 7. The cross-sectional view of the back-projection cone for the uniformly enlarged projection (UEP) and sampling equivalent projection (SEP).

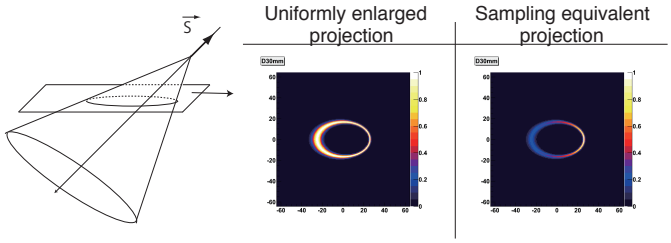


Fig. 8. Same as Fig.7, but a diagonal cross-section.

Among any weighting parameter, $w = 0$ and 2 are characteristic cases. Here, we name the case of $w = 0$ uniformly enlarged projection (UEP) and that of $w = 2$ sampling equivalent projection (SEP), respectively. A comparison of the probability density profile between these methods is shown in Fig. 7, in which two cross-sectional views parallel to a base at differing distances from the apex are presented. For simplicity, the probability at $z = 30$ is normalized. In the UEP, the voxel values are identical anywhere on the cone surface, meaning the profile looks to be uniformly enlarged. Conversely, in the SEP, the same is true for the integral of voxel values within a solid angle as viewed from the apex. For example, the whole integration at a $z = 30$ plane becomes equal to that at $z = 60$ plane. This method corresponds to the projection whereby random sampling of a certain direction is repeated from the spread cone with the Gaussian distribution characterized by $\Delta\theta$. In Fig. 8, we also show the diagonal cross-section for reference.

In our previous study, we tried LM-ML-EM method [11] for the sensitivity $(s_j)$ correction after the SEP, where $s_j$ is the

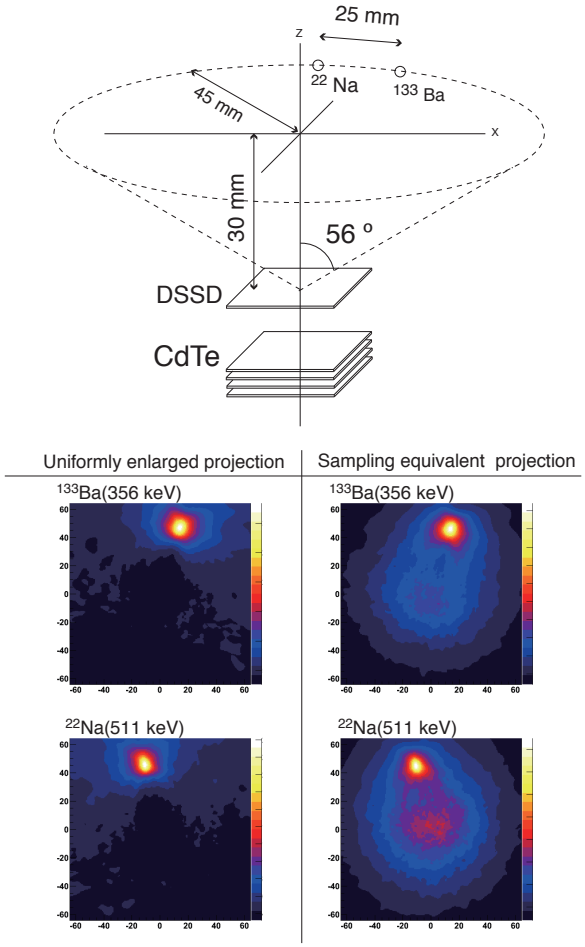


Fig. 9. The UEP and SEP images of $^{133}$Ba (356 keV, 2.8 MBq) and $^{22}$Na (511 keV, 1.3 MBq) point sources at the z=30 mm plane. The sources are located at about 45 mm apart from the center of the camera to verify two back-projection methods.

probability that an event emitted from voxel $j$ is measured, and the event responses derived from the SEP were used during the iteration process. The image quantitativity of phantoms with 2D internal structure was successfully improved [8]. However, for a 3D target such as a mouse, the present data set shows the lack of information as viewed from multi-angle such as SPECTs and PETs, since the prototype camera can not rotate around a target. Therefore, the combination of the SEP and LM-ML-EM method for 3D imaging still needs more careful verification. Conversely, the UEP could be regarded as an approximate way including the sensitivity correction. Because the dominant factor to the position dependance of $s_j$ is the solid angle of the camera looking from the voxel $j$, $s_j$ can be approximately represented as a function of $L^{-2}$. The UEP ($w = 0$) attempts to cancel out the $L^{-2}$ dependance in back-projection process, which is obvious when compared with the SEP ($w = 2$).

Figure 9 shows the resulting UEP and SEP images of $^{133}$Ba (356 keV, 2.8 MBq) and $^{22}$Na (511 keV, 1.3 MBq) point sources located at the z=30 mm plane. The sources are placed 45 mm apart from the center of the camera to verify two back-projection methods. After the back-projection to the three-dimensional space, we picked out the slice where the sources were located. As shown in the right-hand panels, the SEP image is contaminated by "ghost" structure around the camera's center of (0,0). This is because many cones pile up at the very near-field in front of the camera, which unfortunately leads to misunderstanding of the source distribution unless the sensitivity is corrected. Conversely, the UEP relatively evades contamination due to its differences in the probability density profile, aiming the sensitivity correction in back-projection process. Besides, we obtained a reasonable result in the pretest of mouse imaging using the UEP method (see Section IV-A), hence the UEP method was selected for the mouse imaging described in the next section. As noted previously, the application of LM-ML-EM method for 3D imaging needs further experimental studies using 3D phantoms. The data acquisition from multiple angle to reconstruct the 3D source distribution seems to be important, which is planed in future system development.

## IV. MOUSE IMAGING

Having established the Compton camera system and confirmed the near-field back-projection, we tried imaging of multiple radiopharmaceuticals injected into a living mouse to demonstrate the concept of the multi-probe tracker. The location between the mouse and camera is shown in Fig.1. This experiment was conducted at RIKEN, Japan, in collaboration with the Multiple Molecular Imaging Research Laboratory.

### A. Pretest

To determine the accumulation of radiopharmaceuticals in a mouse, it is important to understand the image response. We conducted a pretest by using a point source of $^{133}$Ba (356 keV, 2.8 MBq) in advance of the mouse imaging. In this test, the point source with a diameter of 1.0 mm was placed at a 30 mm plane from the camera and moved with a pitch of 20 mm along the Y-axis as shown in Fig.10 to investigate the imaging response around the mouse's setting position. The observation time at each position is set to take the same livetime of 650 seconds in order to simulate the imaging result of arranged point sources with equivalent intensities.

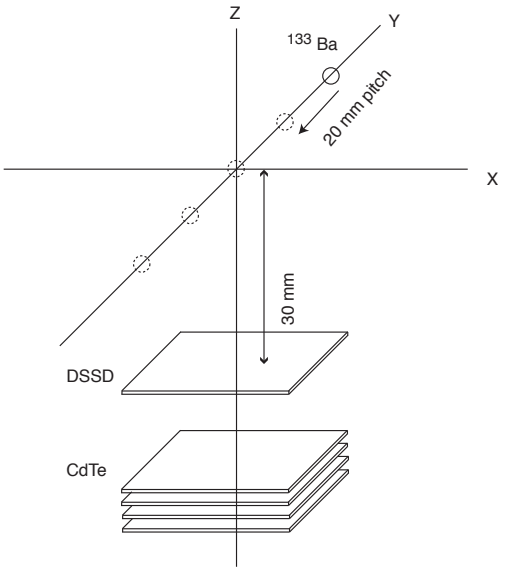


Fig. 10. Setup for the pretest. A $^{133}$Ba (356 keV, 2.8 MBq) point source was moved along the Y-axis with a pitch of 20 mm. The observation time at each position is set to take the same livetime of 650 seconds.

The resulting UEP image picked out at the source's moving plane is shown in Fig.11. First, we indicate that all sources located at (0,-40) (0,-20) (0,0) (0,20) and (0,40) successfully imaged at their correct positions. This is an impressive result because the camera can shoot the whole body of the mouse by fixed point observation. Figure 12 shows a line profile through the center of the points, in which the image responses at each position are shown with different colors. The FWHM of the point spread function (PSF) at the center position is 4.7 mm. As the source shifts away from the center of the camera, the PSF gradually expands and becomes 12 mm at (0,-40) and (0,40). We also confirmed sensitivity correction by the UEP. The ratios of counts to livetime within 350–360 keV window were 1.8 (0,-40), 3.3 (0,-20), 4.5 (0,0), 3.3 (0,20) and 1.8 (0,40) counts/sec at each position, meaning a 44 % drop from the center to the edge. Conversely, the intensities within the region-of-interest (ROI), setting a circle with a radius of 10 mm (see Fig. 11) at each PSF, were 0.89 (0,-40), 0.94 (0,-20), 1 (0,0), 0.94 (0,20) and 0.86 (0,40), where that at (0,0) was normalized to unity, meaning that the sensitivity is well corrected. The absolute detection efficiency, that defined as the probability that a single gamma-ray emitted from the source is detected within the energy window, was 2.6 $\times 10^{-6}$ @ 30 mm, (0,0).

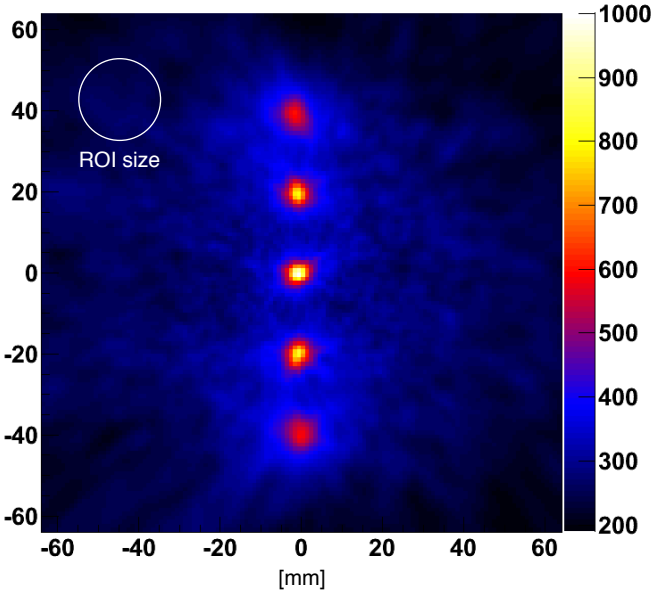


Fig. 11. Resulting UEP image of the preset. The angular uncertainty parameter $\Delta\theta$ is set to 1 degree (see Fig. 6).

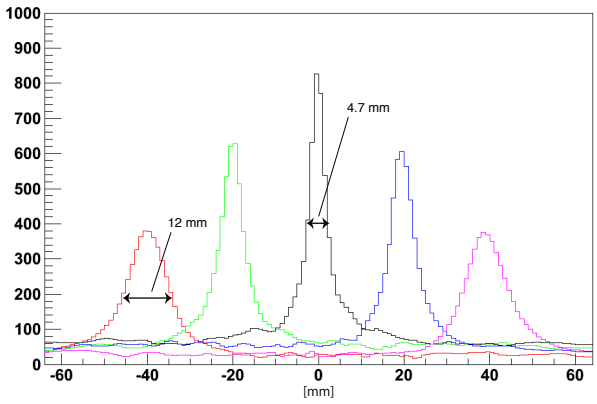


Fig. 12. The line profile through the center of the points, in which the image responses at each position are shown with different colors.

### B. Setting

We use a male 8 week-old ICR mouse in the mouse imaging, into which iodinated ($^{131}$I) methylnorcholestenol produced by FUJIFILM RI Pharma Co., Ltd. and $^{85}SrCl_2$ solution by PerkinElmer Japan Co., Ltd were injected. In order to obtain appropriate accumulation, 18.7 MBq of iodinated ($^{131}$I) methylnorcholestenol was injected three, four and five days before the imaging, respectively, and 2.0 MBq of $^{85}SrCl_2$ solution injected one day before the imaging. The $^{131}$I and $^{85}$Sr emit 364 and 514 keV gamma-rays, respectively.

Iodinated ($^{131}$I) methylnorcholestenol is a widely-used radiopharmaceutical for adrenal scintigraphy. Also, marked accumulation in the thyroid has been identified in rats according to the product sheet [12]. Conversely, since the strontium was taken up in new bone growth as well as calcium, $^{85}$Sr was used for many years in medicine to scan for bone lesions, or tumors [13].

The mouse was set on a heating pad, which was placed at 45 mm underneath the camera, and the observation was conducted for 6 hours. During the imaging, the mouse was kept anesthetized by inhalation of 1.5 % isoflurane and its body temperature was kept at a 37 °C. The energy windows were set to 355–370 and 500–524 keV for $^{131}$I and $^{85}$Sr, respectively. During the back-projection process, the angular uncertainty parameter $\Delta\theta$ was set to 1 degree for both $^{131}$I and $^{85}$Sr. The animal experiments were carried out in compliance with the guidelines for the care and use of laboratory animals and approved by the Committee on Animal Experimentation of RIKEN.

### C. Results

After observation for 6 hours, we obtained $2.93 \times 10^4$ and $8.64 \times 10^3$ counts of Compton event candidates for $^{131}$I and $^{85}$Sr, respectively. The candidates were derived from the energy windows presented in Fig. 13 via the scheme described in section III-A.

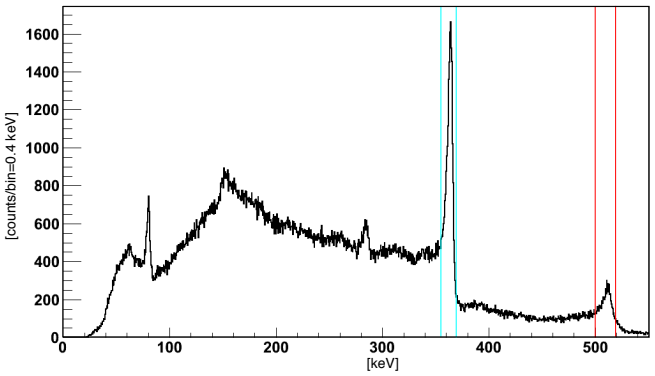


Fig. 13. Energy spectrum obtained by mouse imaging with two energy windows for $^{131}$I (364 keV) and $^{85}$Sr (514 keV)

The accumulation of iodinated ($^{131}$I) methylnorcholestenol (left) and $^{85}$Sr (right) is shown in Fig. 14 with the picture of the subject mouse. The slice image picked out at the plane 40 mm underneath the camera is presented, approximately at the center of the mouse's body. In the case of iodinated ($^{131}$I) methylnorcholestenol, we can see three areas of accumulation around the neck, abdomen and genitals. The accumulations around neck and abdomen are thought to originate from the thyroid and adrenal regions. Intense accumulation was determined around the genitals, which might be from the testicle or prostate. Conversely, accumulations of $^{85}$Sr in new bone growth, such as the skull, spine, lumbar and femur, were clearly identified. The similar accumulations were observed in imaging of another mouse with the some amount of dose injections.

## V. Conclusion and Future Prospects

Although the use of a Compton camera in medical imaging was proposed in the early 1970s and thought to have considerable potential [14], no adequate spatial resolution for medical use has yet been achieved by traditional sensor technologies. Utilizing the prototype Si/CdTe semiconductor Compton camera, we achieved a few mm-level spatial resolution, and successfully imaged distinguishable accumulations of iodinated ($^{131}$I) methylnorcholestenol and $^{85}$Sr injected into a living mouse. The development of a new Si and CdTe strip detector with a pitch of 250 $\mu$m is on going, aiming for improvement of the position resolution up to 1 mm @ 30 mm in the next system.

From these experiments, we also determined two problems to be solved in future developments. One is poor detection efficiency. The efficiency obtained by the prototype is $0.23\times10^{-6}$ (356 keV) @ 10 cm, while that of the existing clinical SPECT system is around $100\times10^{-6}$. Although the efficiency is improved up to $3.4\times10^{-6}$ in the latest Compton camera [15], thirty times' better efficiency is required to arrive at the clinical SPECT system, which could be realized by SGD-base detector configuration [16]. The soft gamma-ray detector (SGD) is a astrophysical Compton camera developing for ASTRO-H satellite mission, and one hundred times' better efficiency than the latest camera is realized by a single detector module (around $400\times10^{-6}$). Arranging several camera modules is also effective because the Compton camera has a very large field of view. Another is to realize three-dimensional imaging. Using mouse imaging, we found that three dimensional information was required to precisely determine the distribution into the mouse's organ around the abdomen and genitals. Multi-angle imaging with a ring-like camera configuration would be required to overcome this problem, according to simulation studies [16].

## Acknowledgments

The authors thank all the staff at RIKEN Multiple Molecular Imaging Research Laboratory for supporting this work.

## References

[1] GE healthcare web site [online].
Available: https://www2.gehealthcare.com/portal/site/usen/gehchome/
[2] ACRORAD web site [online].
Available: http://www.acrorad.co.jp/us/index.html

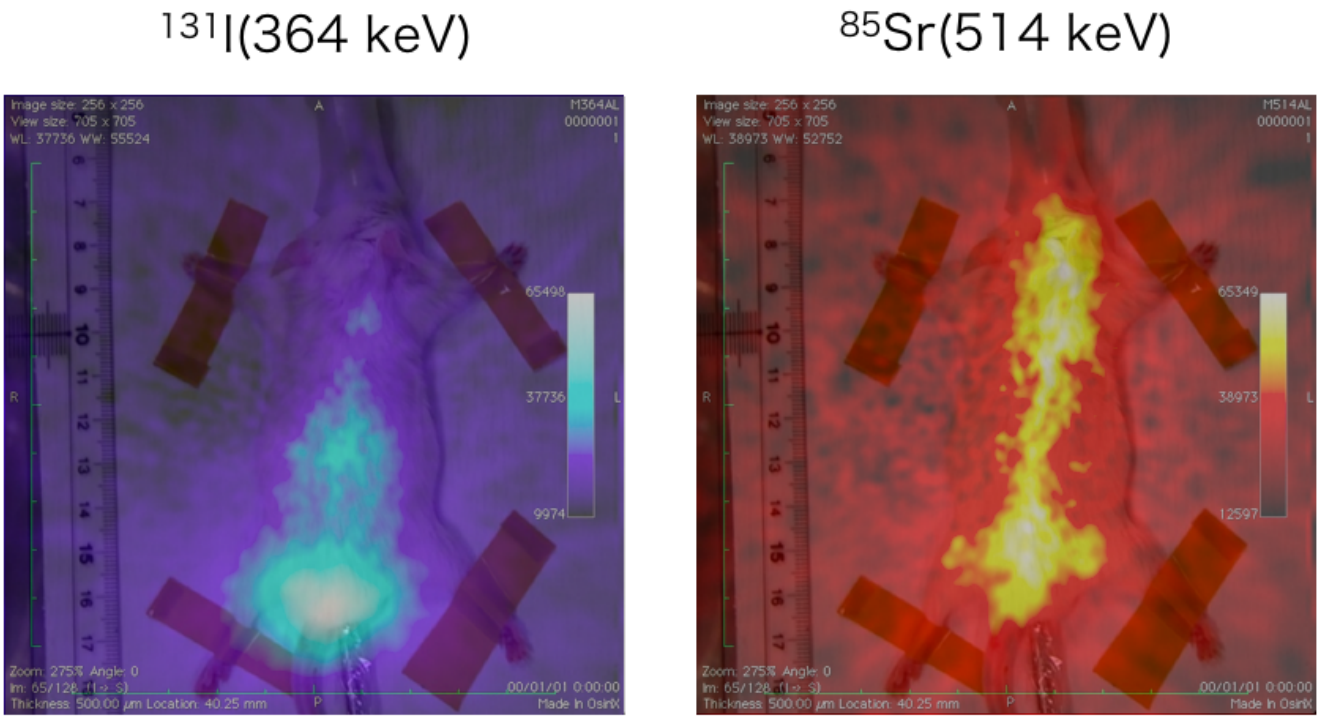


Fig. 14. The accumulation of iodinated ($^{131}$I) methylnorcholestenol (left) and $^{85}$Sr (right) with a picture of the subject mouse


[3] S. Motomura, S. Enomoto, H. Haba, K. Igarashi, Y. Gono and Y. Yano, "Gamma-ray Compton imaging of multitracer in biological samples using strip germanium telescope," IEEE Trans. Nucl. Sci., vol. 54, pp. 710-717, 2007

[4] T. Takahashi, K. Nakazawa, T. Kamae, H. Tajima, Y. Fukazawa, M. Nomachi and M. Kokubun, "High resolution CdTe detectors for the next generation multi-Compton gamma-ray telescope," Proc. SPIE, vol. 4851, pp. 1228-1235, 2003.

[5] S. Watanabe, T. Tanaka, K. Nakazawa, T. Mitani, K. Oonuki, T. Takahashi, T. Takashima, H. Tajima, Y. Fukazawa, M. Nomachi, S. Kubo, M. Onishi and Y. Kuroda, "A Si/CdTe Semiconductor Compton Camera," IEEE Trans. Nucl. Sci., vol. 52, no. 5, pp. 2045-2051, 2005.

[6] T. Takahashi et al., "The ASTRO-H Mission," Proc. SPIE. vol. 7732, pp.77320Z, 2010

[7] ASTRO-H web site [Online]. Available: http://astro-h.isas.jaxa.jp/

[8] S. Takeda, H. Aono, S. Okuyama, S. Ishikawa, H. Odaka, S. Watanabe, M. Kokubun, T. Takahashi, K. Nakazawa, H. Tajima and N. Kawachi, "Experimental results of the gamma-ray imaging capability with a Si/CdTe semiconductor Compton camera," IEEE Trans. Nucl. Sci., vol. 56, no. 3, pp. 783-790, 2009

[9] A. Zoglauer and G. Kanbach, "Doppler broadening as a lower limit to the angular resolution of next - generation Compton telescope," Proc. SPIE-Int. Soc. Opt. Eng., vol. 4851, pp. 1302-1309, 2003

[10] R.C. Rohe, M.M. Sharifi, K.A. Kecevar and C. Bonnerave, "The spatially variant backprojection point kernel function of an energy-subtraction Compton camera for medical imaging," IEEE Trans. Nucl. Sci., vol. 44, no. 6, pp. 2477-2482, 1997

[11] S. Wildermam, N. Clinthorne, J. Fessler, W. Rogers, "List-mode maximum likelihood reconstruction of Compton scatter camera images in nuclear medicine," IEEE Nucl. Sci. Sympo., vol. 3, pp. 1716-1720, 1998

[12] FUJIFIRM RI Pharma web site [Online]. Available: http://fri.fujifilm.co.jp/en/index.html

[13] V. Parsons, M. Williams, D. Hill, P. Frost and A. Lapham, "Strontium-85 scanning of suspected bone disease," Brit. med. Journal, Jan., pp. 19-23, 1969

[14] R.W. Todd, J.M. Nightingale and D.B. Everett "A proposed gamma camera," Nature, vol. 251, pp.132-134, 1974

[15] S. Takeda, Y. Ichinohe, K. Hagino, H. Odaka, T. Yuasa, S. Ishikawa, T. Fukuyama, S. Saito, T. Sato, G. Sato, S. Watanabe, M. Kokubun, T. Takahashi, M. Yamaguchi, H. Tajima, T. Tanaka, K. Nakazawa, Y. Fukazawa and T. Nakano, "Applications and imaging techniques of a Si/CdTe Compton gamma-ray camera," submitted to Physics Procedia

[16] S. Takeda, T. Takahashi, S. Ishikawa, H. Odaka, S. Watanabe, H. Tajima, N. Kawachi and T. Nakano, "Simulation study of 3-D gamma-ray imager with Si/CdTe semiconductor Compton camera," Sensors Applications Symposium (SAS), 2010 IEEE, pp. 170-174, 2010